



HAL
open science

CFD numerical simulation of particle suspension and hydromechanical stress in various designs of multi-stage bioleaching reactors

Jonathan Chéron, Céline Loubière, Stéphane Delaunay, Anne-Gwenaelle Guezennec, Eric Olmos

► To cite this version:

Jonathan Chéron, Céline Loubière, Stéphane Delaunay, Anne-Gwenaelle Guezennec, Eric Olmos. CFD numerical simulation of particle suspension and hydromechanical stress in various designs of multi-stage bioleaching reactors. *Hydrometallurgy*, 2020, 197, pp.105490. 10.1016/j.hydromet.2020.105490 . hal-02968771

HAL Id: hal-02968771

<https://hal.science/hal-02968771>

Submitted on 17 Oct 2022

HAL is a multi-disciplinary open access archive for the deposit and dissemination of scientific research documents, whether they are published or not. The documents may come from teaching and research institutions in France or abroad, or from public or private research centers.

L'archive ouverte pluridisciplinaire **HAL**, est destinée au dépôt et à la diffusion de documents scientifiques de niveau recherche, publiés ou non, émanant des établissements d'enseignement et de recherche français ou étrangers, des laboratoires publics ou privés.



Distributed under a Creative Commons Attribution - NonCommercial 4.0 International License

1 **CFD numerical simulation of particle suspension and hydromechanical stress in various designs of**
2 **multi-stage bioleaching reactors**

3 Jonathan CHERON^a, Céline LOUBIERE^b, Stéphane DELAUNAY^a, Anne-Gwénaëlle GUEZENEC^b, Eric
4 OLMOS^{a,*}

5 ^a Laboratoire Réactions et Génie des Procédés, Université de Lorraine, CNRS, LRGP, 54000 Nancy,
6 France

7 ^b Bureau de Recherches Géologiques et Minières, BRGM, 45100 Orléans, France

8
9 *Corresponding author: eric.olmos@univ-lorraine.fr (E. Olmos).

10

11 **Abstract:** The performance of bioleaching stirred tank reactors (STR) is related to the homogeneity of
12 biomass, substrates and dissolved gases. This work was focused on the characterization of the impeller
13 design on bioreactor hydrodynamics and, more specifically on power, mixing efficiency and particle
14 stress. Few studies addressed the issue of the impact of the impeller design on these, especially for
15 multi-stage bioreactors which are the most commonly used at the industrial scale. To fill this lack, a
16 two-stage solid-liquid computational fluid dynamics (CFD) model was simulated on more than 50
17 conditions to assess power consumption, dissipated power, suspension quality and particle stress. A
18 dual impeller configuration was chosen using Rushton turbines, R600, Hydrofoil, Elephant Ear and
19 HTPG impellers. Grinded pyrite-rich materials (average particles size: 80 μm) were considered as the
20 solid phase at 3 different solid concentrations (10, 18 and 26 % w/w). **Considering the impeller power
21 number (N_p), the configuration with an axial impeller consumed less energy than a radial impeller in
22 concordance with literature data.** The results show that the impeller design had few to no effect on
23 mixing efficiency considering a given power dissipation per unit volume. Independently on the impeller
24 used, unique relationships were found between particle stress and mixing efficiency. This study gives
25 new insights for reactor design and scaling of bioleaching stirred tank reactor and more specifically on
26 the reduction of shear stress for the attached bacterial communities.

27

28 **1. Introduction**

29

30 In the last decades, bioleaching has been successfully implemented at the industrial scale and used,
31 either in the form of dump or heap treatments, or by using large-scale stirred tank reactors (STR) (Clark
32 et al., 2006; Brierley and Brierley, 2013). Dump or heap treatments were widely used for low-grade
33 copper-based sulphides because of the low cost of implementation and maintenance of these
34 processes. On the other hand, bioleaching STR have proven to be more efficient to extract metals from
35 low-grade or refractory ores but are limited to precious metals because of their significant cost of
36 implementation (Rawlings and Johnson, 2007). Nonetheless, bioleaching is evolving towards the
37 exploitation of 'unconventional' resources caused by the declining trend in mean ore grades (Mudd et
38 al., 2013; Frenzel et al., 2017). These resources are represented with unusual features such as very
39 low-grades, complex mineralogy, or high sulphur content. If heap bioleaching has been the main
40 process option for their treatment until now, it is not always suitable. The main reasons that precludes
41 heap application are the composition of the materials to be treated (presence of carbonate causing
42 heap clogging, or high concentrations of sulphides that lead to uncontrolled and excessive
43 temperature increase in the heap) and the lack of sufficient space, especially in densely populated
44 areas like in Europe. In such cases, bioleaching STR might be a technical alternative but is mostly too
45 expensive except in very few cases when the metal value is high enough (e.g. such as in Uganda for the
46 cobalt recovery in flotation tailings (Morin and d'Hugues, 2007) or in Finland for the valorization of
47 nickel from talc mining residues (Wakeman et al., 2011; Neale et al., 2017)). The expansion of STR
48 bioleaching requires thus further technical optimization to reach an economic viability.

49 As in any chemical engineering process, the management of bioleaching bioreactors is aimed at
50 optimizing the reacting conditions to accelerate the oxidation processes of the sulphides and to
51 maximize the solubilization or liberation efficiency of valuable metals. This optimization of the reacting
52 conditions is closely related to the homogeneity of biomass, substrates and dissolved gases throughout
53 the reactor. This is especially important considering that the interactions between the microorganisms
54 and sulphides (microbial attachment and biofilm formation) are considered key parameters to improve
55 bioleaching (Brierley and Brierley, 2013). To this end, improving mixing efficiency would result in a
56 better mass transfer of the components in the system (Petersen, 2010; Buffo et al., 2016).
57 Furthermore, significant power consumption of the process comes from mechanical mixing, which is
58 directly related to the solid content (through sufficient agitation rate ensuring suspension and gas-
59 liquid mass transfer efficiency) and its physical properties (Bujalski et al., 1999; Jafari et al., 2012).
60 Bioleaching in STR involves substantial power consumption, which results in high operating costs that
61 limit, until now, the use of this technology to the treatment of high added-value resources (mainly
62 refractory gold ores). Besides these commodities, the expansion of bioleaching to 'unconventional'
63 primary resources with lower value, such as low-grade ores or base metal ores and tailings, requires
64 adapting the STR process to the characteristics of these resources in order to limit investment and
65 operating costs while maintaining high extraction efficiency (Bouquet and Morin, 2006; Morin and
66 d'Hugues, 2007) as these resources present a wide range of shape, size and physical properties.

67 Solid-liquid stirred tanks were widely studied in the literature to define standard designs in order to
68 optimize their efficiency through a better solid distribution (Montante et al., 2012; Tamburini et al.,
69 2014). The power consumption per unit of volume P/V is generally considered as one of the best
70 criterion for the scale-up of these vessels (Rushton, 1950; Chapple et al., 2002) as it could be related
71 to mass transfer capacities or mixing times (Bouaifi and Roustan, 2001; Zhang et al., 2017). Dimensional
72 analysis indicates that its value is provided by dimensionless models relating the power number N_p to
73 the Reynolds number Re , the impeller power number N_p being represented by the following equation:

$$N_p = \frac{P}{\rho_l N^3 D^5} = f \left(Re = \frac{\rho_l N D^2}{\mu} \right) \quad (1)$$

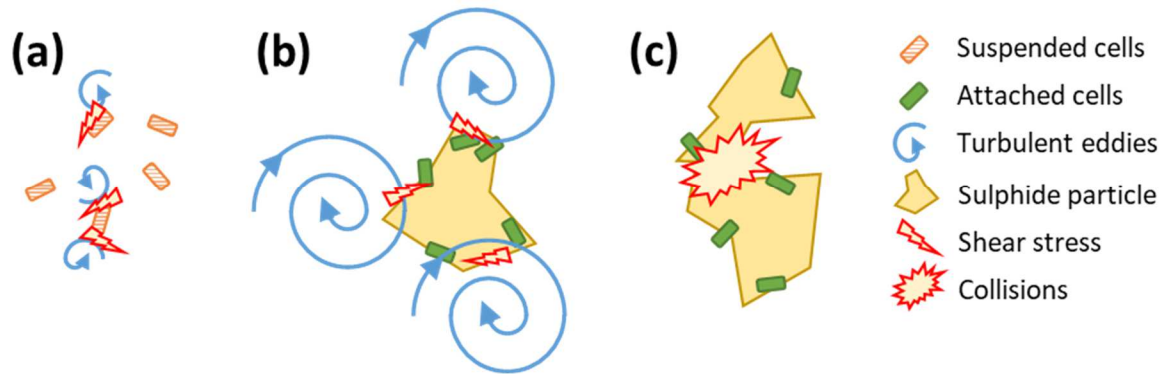
74 with P the power required for the impeller rotation, ρ_l the fluid density, N the agitation rate, μ the
75 liquid viscosity and D the impeller diameter. It is a well-known result that, in baffled vessels, the power
76 number is independent of the Reynolds number in the turbulent regime ($Re > 10^4$) and reaches a
77 constant value that only depends on bioreactor design (Rushton, 1950). It is also important to
78 emphasize that the required power P (which is related to the electric power consumption) should be
79 preferentially minimized to limit the OPEX of the bioleaching process.

80 Nevertheless, this parameter is not sufficient to describe the suspension quality, defined by the spatial
81 distribution of the particles within the flow. To describe the suspension quality, the just-suspended
82 agitation rate N_{js} , defined as the minimal agitation rate ensuring the suspension of all solid particles,
83 has often been used as a good compromise between optimal mass transfer and minimal power
84 consumption (Zwietering, 1958; Brucato et al., 2010; Tamburini et al., 2012, 2011). However, this
85 criterion fails to describe the solid suspension quality (Harrison et al., 2012). Mak (1992) used the
86 standard deviation of the local solid concentration as a way to characterize the solid distribution but
87 the experimental set-up complexity makes difficult the use of this method to screen a high number of
88 bioreactor designs. Furthermore, the solid distribution within the liquid phase should be related to the
89 local values of turbulent dissipation rates (Kumaresan and Joshi, 2006) which strongly depend on both
90 the vessel and the impeller design (Houcine et al., 2000). However, while an increase of power
91 dissipation is expected to sensibly improve the mixing efficiency of the bioreactor from a physical point
92 of view, the hydromechanical stress generated by the agitation may also weaken the microbial
93 adhesion or even lower the process performances. This is particularly detrimental for bioleaching

94 processes due to the major importance of microbial attachment and biofilm formation (Rodríguez et
95 al., 2003; Guezennec et al., 2017). This was observed with *Acidithiobacillus ferrooxidans* cultures in
96 shaking flasks (Xia et al., 2008). Similar observations were made in STR during thermophilic cultures of
97 *Sulfolobus* sp. (d'Hugues et al., 2002; Sissing and Harrison, 2003). Moreover, it was shown by Wang et
98 al. (2014) that, for moderately thermophiles cultures, the proportion of attached cells is higher than
99 of planktonic cells. Also, altering the capacity of the cell to attach on the mineral surface leads to a
100 decrease of bioleaching efficiency (d'Hugues et al., 2008). Considering the effect of solid loading, it was
101 demonstrated by Witne and Phillips (2001) that the increase of solid concentration in continuous STR
102 induced an increase of the leaching rate until a point where it had a negative effect, which could be
103 caused by the attrition of cells. Similar results were observed by Raja (2005) in shaking bottles where
104 a decrease in specific oxygen consumption rate and cell viability was observed at increasing quartzite
105 concentrations. In the same way, Nemati and Harrison (2000) observed that if a partial suspension of
106 the pulp was obtained for a concentration of 18 % w/v (corresponding to 16 % w/w with the hypothesis
107 of $\rho_s = 2610 \text{ kg m}^{-3}$), the rate of iron solubilization was reduced. However, achieving complete particle
108 suspension led to an apparent cell damage, as shown by a reduced cell count. More generally, it must
109 be underlined that solid concentration has not the same influence on mesophilic and moderately
110 thermophilic bacteria (such as *Leptosirillum* and *Acidithiobacillus* sp.), and extremely thermophilic
111 archaea (such as *Acidianus*, *Metallosphaera*, and *Sulfolobus* sp.). As reviewed by Brierley and Brierley
112 (2013), STR bioleaching with archaea, which have no rigid cell wall, necessitates a somewhat lower
113 solid concentration than 12.5 % in reactor opposed to the common 20 % in plants processing sulfidic-
114 gold concentrates with mesophilic and moderately thermophilic bacteria, due to their difference of
115 shear sensitivity.

116 To understand the previous results, it is important to consider that, in bioleaching reactors,
117 hydromechanical stresses may impact the process performance following three phenomena: (i) direct
118 shear of the liquid phase on the microorganisms in suspension (Fig. 1a), (ii) shear stress on particles
119 that potentially hold adhered microorganisms or biofilms (Fig. 1b), and (iii) particle-particle frictions
120 and collisions (Fig. 1c). The occurrence of direct shear is still debated. It is generally assumed, but not
121 completely demonstrated, that hydrodynamics has no impact on planktonic microorganisms if, locally,
122 the Kolmogorov length scale $l_K = (\nu^3/\varepsilon)^{0.25}$ is higher than the microorganism diameter (Nienow,
123 2006). In this equation, ε (W kg^{-1}) is the power dissipation per unit of mass (or turbulent dissipation
124 rate) and ν is the kinematic viscosity ($\text{m}^2 \text{s}^{-1}$). Considering microorganisms of the micrometer scale, the
125 maximal power dissipation necessary to induce direct cell damage would be $\varepsilon \sim 10^6 \text{ W kg}^{-1}$, which is
126 unlikely to be reached in standard stirred tank bioreactors. In comparison, the value of power
127 dissipation that would induce hydrodynamic stress on particle with a diameter in the range 10-100 μm
128 would be $\varepsilon \sim 0.01\text{-}100 \text{ W kg}^{-1}$, which is more likely to be observed with usual mixing conditions. Lastly,
129 particle-particle frictions frequency and intensity depend on the local volume fraction of particles and
130 the relative velocity between particles, and consequently on the design of the bioreactor, the agitation
131 rate and the mean particle concentration.

132



133

134

135

Fig. 1: Description of the hydromechanical stress applied on microorganisms due to: (a) direct shear of the liquid; (b) shear stress on particles; (c) particle-particle frictions and collisions.

136

137

138

139

140

141

142

143

144

145

146

147

148

149

150

151

152

From a physical point of view, a quantitative description of the bioreactor hydrodynamics relies on a better knowledge of the coupling between bioreactor design, operating conditions, solid distribution within the bioreactor and particle stress. Computational Fluid Dynamics (CFD) can be used as an efficient approach to locally represent or calculate the hydrodynamics parameters of these processes. Among others, the local solid concentration, the liquid mean and fluctuating velocities and the impeller torque are representative parameters (Wadnerkar et al., 2012; Zheng et al., 2018b). In a gas-mixed leaching tank, Song et al. (2015) used a gas-liquid Euler-Euler approach to enhance the design of the reactor in terms of bubble diameter or draft tube diameter. In the study of Gradov et al. (2017), the rheology of the slurry was modelled using a power law while a gas-liquid Euler-Euler approach was used to determine the volumetric distribution of the gas-liquid mass transfer coefficient within the bioreactor. Three-phase flow was simulated in a vessel equipped with an HEDT impeller by Zheng et al. (2018a) ; the authors showed that a gas-liquid-solid Euler-Euler-Euler combined with a $k - \varepsilon$ turbulence model was able to predict the mechanical power dissipation with an error lower than 15 %. Recently, Loubière et al. (2019) developed strategies to determine optimal bioreactor configurations for the culture of mesenchymal stem cells in stirred tank vessels, on spherical microcarriers by using a coupled CFD-genetic algorithm approach. The optimization criterion was a minimization of power dissipation encountered by the particles, at the particle just-suspended state.

153

154

155

156

157

158

159

160

161

162

163

164

Despite the referenced studies, the identification of the impact of impeller geometry choice on bioleaching reactor hydrodynamics remains incomplete, especially in multi-stage bioreactors, which are the most commonly used at the industrial scale. Moreover, no studies put into evidence the coupling between power dissipation, solid homogeneity and occurrence of particle stress. The present work was focused on the comparison of the effects of the impellers design on the hydrodynamics of a two-stage solid-liquid bioleaching reactor. For this, more than 50 CFD simulations based on a liquid-solid granular Euler-Euler model were carried-out with six radial and axial impeller designs. The performance of each impeller was quantified through the power number N_p and compared with literature data. Furthermore, the standard deviation of the solid concentration distribution was calculated to determine the respective efficiency of the impellers on solid scattering. The spatial distribution of hydromechanical stress on particles was determined for each bioreactor configuration and for three solid concentrations of 10, 18 and 26 % w/w.

165

166

167

2. Material and Methods

2. 1. Model description

168 In this work, a steady-state Eulerian-Eulerian multiphase approach was used to simulate the solid-
 169 liquid flow, where the continuous and dispersed phases are considered as interpenetrating continua.
 170 Both phases are identified by their own volume fraction and are related as:

$$\alpha_s + \alpha_l = 1 \quad (2)$$

171 where α_s and α_l are the volume fractions of the solid and liquid phases respectively. The continuity
 172 equation for each phase can be written as:

$$\nabla \cdot (\alpha_l \rho_l \mathbf{u}_l) = -\nabla(\gamma_s \nabla \alpha_s) \quad (3)$$

$$\nabla \cdot (\alpha_s \rho_s \mathbf{u}_s) = \mathbf{F}_{TD} = \nabla(\gamma_s \nabla \alpha_s) \quad (4)$$

173 where ρ and \mathbf{u} are the density and velocity of each phase, and \mathbf{F}_{TD} is related to the turbulent dispersion
 174 force. This turbulent dispersion force takes into account the dispersion due to turbulent velocity
 175 fluctuations and was modelled using the diffusion-in-VOF model. The diffusion coefficient γ_s is related
 176 to the turbulent viscosity $\mu_{t,l}$ by $\gamma_s = (\mu_{t,l}/0.75)$. The momentum conservation equation for each
 177 phase is:

$$\nabla \cdot (\alpha_l \rho_l \mathbf{u}_l \mathbf{u}_l) = -\alpha_l \nabla p + \alpha_l \rho_l \mathbf{g} + \nabla \cdot \bar{\bar{\boldsymbol{\tau}}}_l + \mathbf{F}_{D,ls} \quad (5)$$

$$\nabla \cdot (\alpha_s \rho_s \mathbf{u}_s \mathbf{u}_s) = -\alpha_s \nabla p - \nabla p_s + \alpha_s \rho_s \mathbf{g} + \nabla \cdot \bar{\bar{\boldsymbol{\tau}}}_s - \mathbf{F}_{D,ls} \quad (6)$$

178 where p is the pressure field shared by the two phases, p_s is the solid pressure, \mathbf{g} the gravitational
 179 acceleration, $\bar{\bar{\boldsymbol{\tau}}}$ the phase stress strain tensor and $\mathbf{F}_{D,ls}$ the interphase momentum transfer.

180 Interphase forces that are generally expected in a multiphase liquid-solid flow include: turbulent
 181 dispersion, drag, virtual mass, Basset and lift forces. Previous studies have shown that solid-liquid flows
 182 in STR are correctly represented using only turbulent dispersion and drag forces with a low effect of
 183 other forces on simulation results (Ljungqvist and Rasmuson, 2001; Khopkar et al., 2006; Qi et al.,
 184 2013). The turbulent dispersion force \mathbf{F}_{TD} should be modelled when the size of turbulent eddies is
 185 larger than the particle size (Kasat et al., 2008; Wadnerkar et al., 2012) which is *a priori* expected in
 186 standard bioreactors. Furthermore, the virtual mass, Basset and lift forces may be neglected as they
 187 have a much lower magnitude than the drag forces. (Tatterson, 1991; Tamburini et al., 2014; Raja
 188 Ehsan Shah et al., 2015).

189 The drag force $\mathbf{F}_{D,ls}$ between liquid and solid phases was calculated by the following equation:

$$\mathbf{F}_{D,ls} = K_{ls}(\mathbf{u}_s - \mathbf{u}_l) \quad (7)$$

190 with K_{ls} the interphase exchange coefficient between liquid and solid phases respectively, determined
 191 by:

$$K_{ls} = C_{D,ls} \frac{3}{4} \rho_l \frac{\alpha_s \alpha_l}{d_p} |\mathbf{u}_s - \mathbf{u}_l| \quad (8)$$

192 The drag coefficient $C_{D,ls}$ is given by the Schiller and Naumann model (Schiller, 1933):

$$C_{D,ls} = \begin{cases} 24(1 + 0.15Re_p^{0.687})/Re_p & Re_p < 1000 \\ 0.44 & Re_p \geq 1000 \end{cases} \quad (9)$$

193 with Re_p the particle Reynolds number:

$$Re_p = d_p(\mathbf{u}_s - \mathbf{u}_l)/\nu_l \quad (10)$$

194 The dispersed $k - \varepsilon$ model was chosen as it is recommended for multiphase flows considering a
 195 continuous and a dispersed phases with a density ratio between phases equal or higher to 2.5 (s.n.

196 Ansys, 2019). This is often validated in bioleaching as most substrates are sulphidic materials of density
 197 higher than 2.5. In our case, water was chosen as the liquid phase ($\rho_l = 1000 \text{ kg m}^{-3}$, $\mu_l = 0.001 \text{ Pa s}$)
 198 and particles with the characteristics of grinded pyrite-rich materials ($\rho_s = 2610 \text{ kg m}^{-3}$, $d_p = 80 \text{ }\mu\text{m}$,
 199 pyrite fraction = 51 %) were considered for the solid phase. In this approach, turbulence is fully-
 200 modelled for the continuous phase and the turbulence of the dispersed phase is possibly taken into
 201 account through additional interaction terms. The $k - \varepsilon$ model provides the transport equations of
 202 the turbulent kinetic energy k and its dissipation rate ε :

$$\nabla \cdot (\alpha_l \rho_l \mathbf{u}_l k_l) = \nabla \cdot \left(\alpha_l \left(\mu_l + \frac{\mu_{t,l}}{\delta_k} \right) \nabla k_l \right) + \alpha_l G_{k,l} - \alpha_l \rho_l \varepsilon_l \quad (11)$$

$$\nabla \cdot (\alpha_l \rho_l \mathbf{u}_l \varepsilon_l) = \nabla \cdot \left(\alpha_l \left(\mu_l + \frac{\mu_{t,l}}{\delta_\varepsilon} \right) \nabla \varepsilon_l \right) + \alpha_l \frac{\varepsilon_l}{k_l} (C_{\varepsilon 1} G_{k,l} - C_{\varepsilon 2} \rho_l \varepsilon_l) \quad (12)$$

203 $\mu_{t,l}$ is the turbulent viscosity of the continuous liquid phase:

$$\mu_{t,l} = \rho_l C_\mu \frac{k_l^2}{\varepsilon_l} \quad (13)$$

204 $G_{k,l}$ is the term of production of turbulent kinetic energy and the constants are defined as follow:
 205 $C_\mu = 0.09$, $C_{\varepsilon 1} = 1.44$, $C_{\varepsilon 2} = 1.92$, $\delta_k = 1$ and $\delta_\varepsilon = 1$.

206 Lastly, no additional interaction terms were taken into account for turbulence as preliminary
 207 simulations showed no impact of these terms on simulation results (data not shown).

208 The particle-particle interactions were modelled by the kinetic theory of granular flows, which is an
 209 extension of the model for molecular motion in a dense gas phase. It aims at determining the solid
 210 pressure p_s which represents the normal forces due to particle interactions. From the kinetic theory,
 211 Jenkins and Savage (1983) proposed that this solid pressure is the sum of a kinetic energy term and of
 212 one term that includes the particle-particle collisions:

$$p_s = \alpha_s \rho_s \theta_s + 2\rho_s (1 + e_{ss}) \alpha_s^2 r_0 \theta_s \quad (14)$$

213 The coefficient of restitution of particle collision e_{ss} is set to 0.9. The granular temperature θ_s is a
 214 measure of the kinetic energy due to the fluctuating velocities u'_s of the particles:

$$\theta_s = \frac{1}{3} u'_s{}^2 \quad (15)$$

215 Neglecting the convective and diffusive transports, the transport of the granular temperature within
 216 the bioreactor is provided by Ding and Gidaspow (1990):

$$(-p_s \bar{\mathbf{I}} + \bar{\boldsymbol{\tau}}_s) : \nabla \mathbf{u}_s - \gamma_{\theta_s} + \Phi_{ls} \quad (16)$$

217 First-term of the left-hand side represents the generation of fluctuating energy due to the solid
 218 pressure and viscous force; the second term is the dissipation of the fluctuating energy and the last
 219 term is the exchange of fluctuating energy between liquid and solid phases respectively. The transfer
 220 of fluctuating energy is given by:

$$\Phi_{ls} = -3K_{ls} \theta_s \quad (17)$$

221 The collisional dissipation of energy γ_{θ_s} is provided by:

$$\gamma_{\theta_s} = \frac{12(1 - e_{ss}^2) r_0}{d_p \pi^{0.5}} \rho_s \alpha_s^2 \theta_s^{3/2} \quad (18)$$

222 The radial distribution function r_0 is a correction factor that modifies the probability of collisions
 223 between particles when the solid granular phase becomes dense:

$$r_0 = \frac{a + d_p}{a} \quad (19)$$

224 with a the distance between the particles. In our case, this distribution is determined by:

$$r_0 = \left[1 - \left(\frac{\alpha_s}{\alpha_{s,\max}} \right)^{1/3} \right]^{-1} \quad (20)$$

225 with $\alpha_{s,\max} = 82$ % w/w (corresponding to 63 % v/v), the particle packing limit.

226 The solid shear stress tensor $\bar{\tau}_s$ arises from particle momentum exchange due to translations and
 227 collisions and depends on the solid viscosity:

$$\bar{\tau}_s = \mu_s \nabla \mathbf{u}_s = (\mu_{s,\text{col}} + \mu_{s,\text{kin}}) \nabla \mathbf{u}_s \quad (21)$$

228 The collisional contribution to the shear viscosity is given by:

$$\mu_{s,\text{col}} = \frac{4}{5} \alpha_s \rho_s d_p r_0 (1 + e_{ss}) \left(\frac{\theta_s}{\pi} \right)^{1/2} \quad (22)$$

229 And the kinetic viscosity by:

$$\mu_{s,\text{kin}} = \frac{10 \rho_s d_s \sqrt{\theta_s \pi}}{96 \alpha_s (1 + e_{ss}) r_0} \left[1 + \frac{4}{5} r_0 \alpha_s (1 + e_{ss}) \right]^2 \quad (23)$$

230

231 *2. 2. Simulation setup*

232 The geometry setup for the simulation of the lab-scale bioreactor is shown on Fig. 2; this bioreactor is
 233 routinely used for bioleaching experiments. The tank was a cylindrical vessel of diameter $T = 0.12$ m
 234 and liquid height $H = 0.187$ m. The tank was equipped with four conical baffles of width equal to $T/10$,
 235 placed symmetrically.

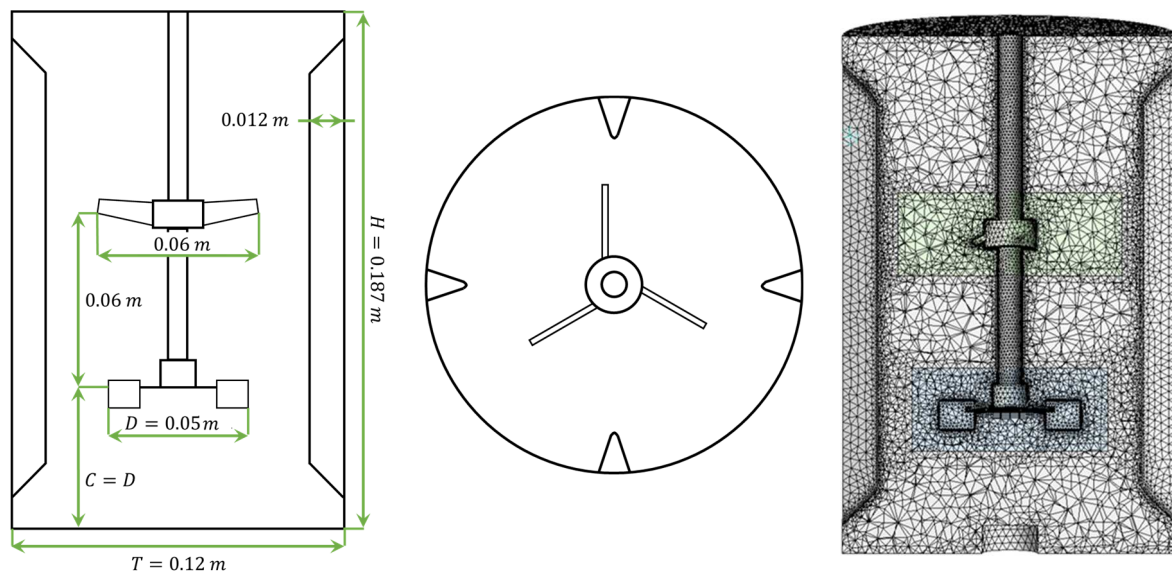
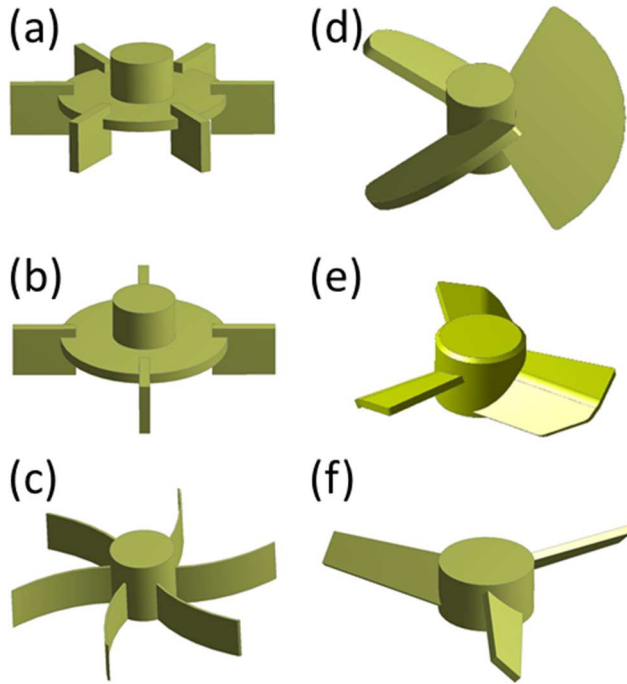


Fig. 2: Planar view (left), cross-section (middle) and mesh (right) of the two-stage stirred tank reactor.

236 A dual impeller configuration was chosen using various bottom impeller designs but a fixed design for
 237 the top impeller (Fig. 3). Considering the height on tank diameter ratio, the choice of a multi-stage
 238 design is recommended to provide sufficient liquid mixing near the surface. As the focus was put on
 239 particles suspension and stress, and to limit the number of configurations simulated, only the bottom
 240 impeller design was modified. The bottom impellers had a fixed diameter $D = 0.05$ m with an off-
 241 bottom clearance $C = D$. The top impeller, a three-blade hydrofoil (A310), was positioned at a spacing
 242 $S = 0.06$ m above the bottom impeller and had a diameter equal to 0.06 m.



243

244 Fig. 3: Impellers used in simulations. (a) 6-bladed Rushton turbine (RT6B); (b) 4-bladed Rushton turbine
 245 (RT4B); (c) R600 spiral backswept impeller (R600); (d) Elephant-Ear impeller operating in down-
 246 pumping mode (EEed); (e) HTPG impeller operating in down-pumping mode (HTPGd); (f) Lightnin A310
 247 impeller operating in up-pumping mode (A310).

248 Each impeller configuration was simulated at 6 different agitation rates ($N = 200, 300, 400, 500, 600$
 249 and 700 rpm), ensuring fully turbulent conditions for each case ($10^4 < Re < 5 \times 10^4$). Moreover, the
 250 impact of the solid concentration on solid-liquid suspension was also determined by fixing three
 251 different solid concentrations: 10, 18 and 26 % w/w. A non-uniform mesh structure was created to
 252 divide the geometry setup using the Fluent Meshing tool and was composed of 400,000 tetrahedral
 253 elements. Refinements were done along the wall and in the impellers regions. Mesh independence
 254 was preliminary verified by comparing velocity vectors fields and volume-averaged power dissipation.

255 2. 3. Power consumption

256 To obtain the power number N_p defined in eq. (1), the power consumption P was calculated by the
 257 following equation:

$$P = 2\pi N C_w \quad (24)$$

258 with N the agitation rate and C_w the impeller torque, which was determined by the numerical
 259 simulations. Mechanical energy balance within the bioreactor imposes that the power consumption P
 260 should be of the same order of magnitude as the dissipated power P_{diss} determined by the turbulence
 261 model:

$$P_{diss} = \rho_l \langle \varepsilon \rangle V_l \quad (25)$$

262

263 2. 4. Solid dispersion

264 Solid dispersion is a key process parameter in solid-liquid bioreactors as it strongly impacts the mass
 265 transfer to the particles but also the microenvironment of substrates around the particles. One way to
 266 determine the suspension quality is to use the Zwietering correlation which models the just-suspended

267 agitation rate of the particles N_{js} in the bioreactor (based on the Zwietering criterion that considers
 268 the particles as they do not remain settled more than 2 seconds near the vessel bottom at the just-
 269 suspended state). It is generally assumed that the bioreactor and impeller geometries have an impact
 270 on N_{js} but also on the operating conditions of the process:

$$N_{js} \propto v_l^{0.1} \left[\frac{g(\rho_s - \rho_l)}{\rho_l} \right]^{0.45} \cdot X^{0.13} d_p^{0.2} D^{-0.85} \quad (26)$$

271 Thus, for a given bioreactor configuration and operating conditions, the scaling law $N_{js} \propto X^{0.13}$ should
 272 be obtained. Despite the interest of determining this criterion, it is insufficient if the distribution of
 273 particle concentrations or stresses are also looked for. One way to improve the description of the
 274 particles suspension behaviour is to determine the suspension quality H_s which can be calculated as
 275 the volume-averaged difference between the local and the mean concentration of solid particles (Mak,
 276 1992; Khopkar et al., 2006; Murthy et al., 2007; Hosseini et al., 2010). This parameter is determined
 277 using the local fraction of each elements of the mesh:

$$H_s = 1 - \sqrt{\frac{1}{V_{tot}} \cdot \iiint_{V_{tot}} (\alpha_s - \langle \alpha_s \rangle)^2 dV} \quad (27)$$

278 where α_s denotes the local volume fraction of the solid phase and $\langle \alpha_s \rangle$ represents the volume-
 279 averaged value of particle concentration in the vessel. This value of H_s had to be adjusted to take into
 280 account the packing limit of the particles given by the maximal local solid concentration of 82 % w/w:

$$H_{s,adj} = \frac{H_s - H_{s,min}}{H_{s,max} - H_{s,min}} \quad (28)$$

281

282 where $0.75 < H_{s,min} < 0.85$ and $H_{s,max} = 1$ are respectively the minimal and maximal values of H_s for
 283 $\alpha_s = \alpha_{s,max} = 0.82$ and $\alpha_s = \alpha_{s,min} = \langle \alpha_s \rangle$. The value of $H_{s,min}$ is dependent on the volume-
 284 averaged concentration of particles considered in the calculations.

285 2. 5. Solution method

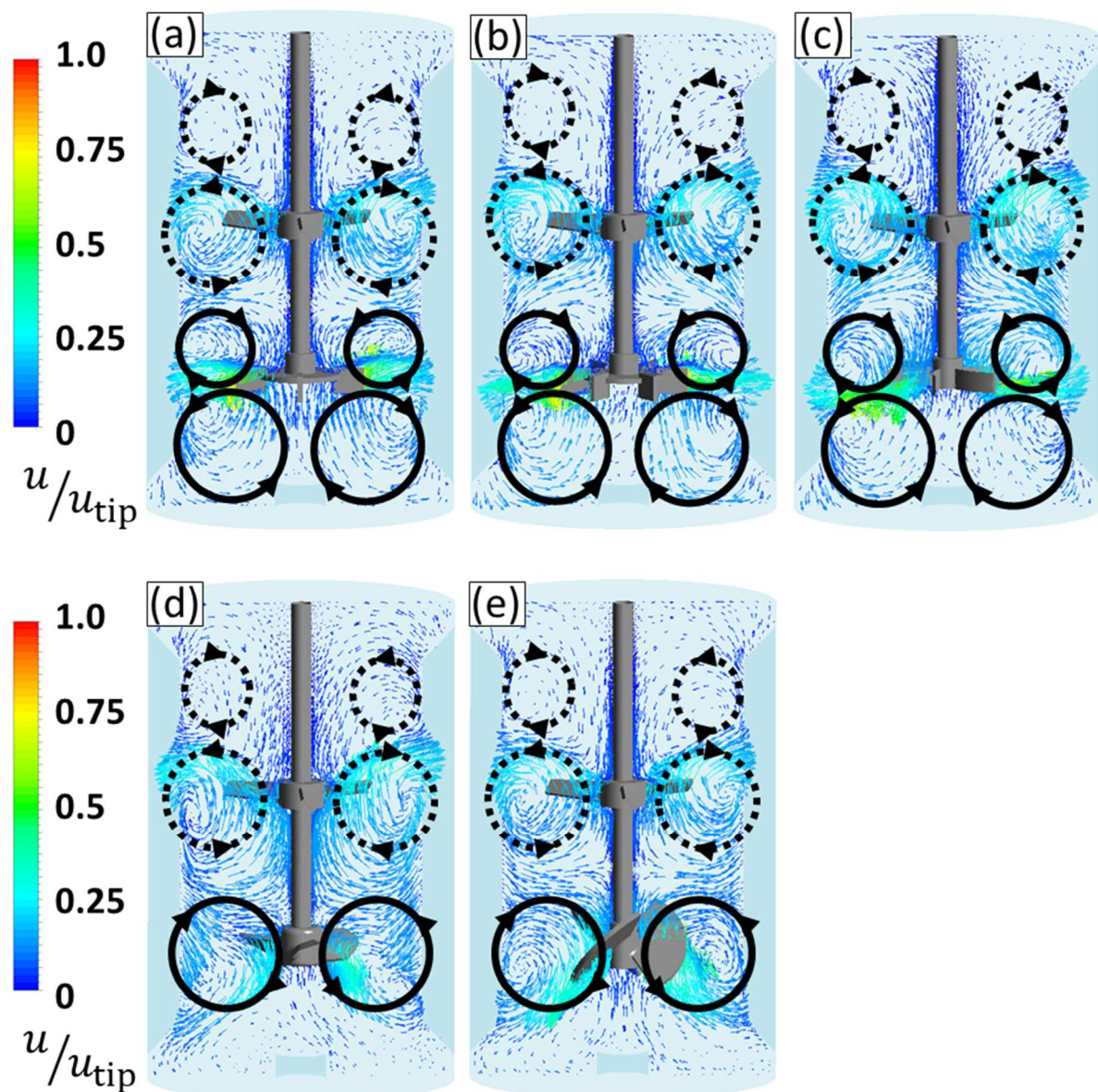
286 The commercial software ANSYS Fluent 2019R3 was used for the numerical simulation of the
 287 multiphase flow. The conservation equations presented in Eq. (2-23) were applied in all meshes and
 288 were solved using the steady-state Eulerian method. The impellers rotation was modelled using the
 289 multiple reference frame approach. The rotating domain was positioned at $r_{bottom} = 0.035$ m, 0.036
 290 $m \leq z_{bottom} \leq 0.066$ m and $r_{top} = 0.040$ m, 0.096 m $\leq z_{top} \leq 0.126$ m, respectively for the bottom and
 291 the top impellers. The pressure-velocity based solver using the SIMPLE algorithm was used to solve the
 292 set of conservation equations. Discretization of the mass, momentum and volume fraction equations
 293 was carried-out using the second-order upwind scheme while pressure was spatially discretized using
 294 the PRESTO! scheme (s.n. Ansys, 2019). Convergence of the simulations was admitted when transport
 295 equations residuals were less than 10^{-3} and when the local solid volume fraction reached a steady state
 296 at three locations of the vessel ($r = 0.025$ m and $z = 0.025, 0.090$ and 0.160 m).

297

298 3. Results and discussion

299 3.1. Liquid flow patterns

300 Firstly, to validate the accuracy of the CFD model, the flow patterns were qualitatively compared with
 301 data from the literature. The dimensionless liquid velocity profiles shown in Fig. 4 present the flow
 302 patterns induced by the dual-impellers bioreactor. The top A310 showed the predicted pattern of a
 303 mixed flow, presenting a one-loop flow pattern as it operates in up-pumping mode, which was also
 304 shown by Vrabel et al. (2000) on a multiple impellers configuration. The proximity of the liquid surface
 305 promoted the formation of two supplementary liquid loops. For the bottom impeller, various flow
 306 patterns were observed depending on the impeller used: the radial impellers (RT4B, RT6B and R600)
 307 generated a two-loop pattern with a radial ejection of the liquid towards the reactor wall while the
 308 down-flow axial impellers (HTPGd and EEd) showed a single-loop flow pattern. These results agreed
 309 with the experimental results of previous studies as similar flow patterns were shown for radial
 310 impellers by Zhang et al. (2017) and for down-flow axial impellers by Bouaifi and Roustan (2001). As
 311 expected, the choice of the tip speed $u_{tip} = \pi ND$ as a representative design parameter is highly
 312 questionable, as shown by the variability of the flow pattern from one configuration to another
 313 (Nienow, 2006).



314 Fig. 4: Normalized liquid velocity vectors profiles at 500 rpm for: (a) the RT4B-A310 configuration; (b)
 315

316 the RT6B-A310 configuration; (c) the R600-A310 configuration; (d) the HTPGd-A310 configuration; (e)
317 the EEd-A310 configuration. The tip speed was given by $u_{\text{tip}} = \pi ND$.

318 3.2. Power consumption

319 The power numbers of each impeller were calculated using eq. (1) for each agitation rates and solid
320 concentrations and the mean value obtained and standard deviation were compared with data from
321 literature, as shown in Table 1.

322 Table 1. Mean value and standard deviation of the calculated impeller power numbers for each
323 impeller configuration used and comparison with data from literature (referenced N_p).

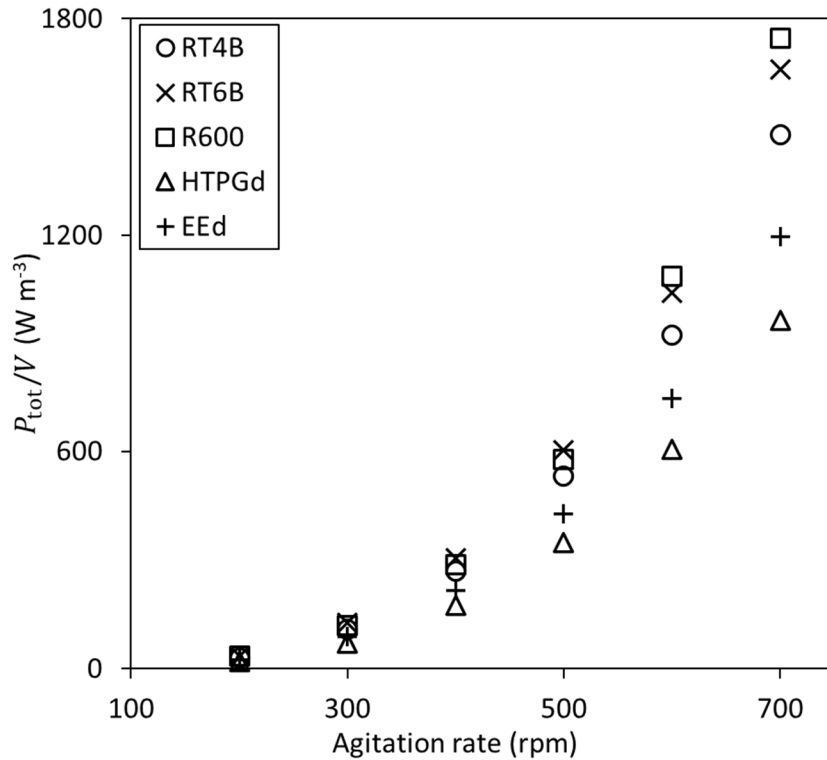
Impeller	Calculated N_p	Referenced N_p	Literature reference
RT4B	3.1 ± 0.1	4.0	Roustan (2005)
RT6B	4.0 ± 0.1	4.0 - 6.0	Chapple et al. (2002)
R600	3.6 ± 0.3	4.2	Roustan (2005)
HTPGd	0.73 ± 0.07	0.67	Roustan (2005)
EEd	1.9 ± 0.1	1.7 - 2.1	Zhu et al. (2009); Loubière et al. (2019)
A310	0.76 ± 0.05	0.3 - 0.5	Kumaresan and Joshi (2006)

324

325 The results showed that for fully turbulent conditions, the variation of agitation rates induced few
326 variations of the power numbers compared to the expected values, as classically expected in turbulent
327 regime (Rushton, 1950; Furukawa et al., 2012). Moreover, the predicted values of N_p , calculated for
328 each impeller in the two-stage configurations, are similar to those reported for single-impeller
329 configurations meaning that the total power consumption is approximately equal to the additive
330 power consumption of both impellers. This can be explained by the fact that, with enough spacing
331 between the impellers ($S/D > 1$), the respective dissipated power of the impellers in a two-stage
332 reactor is similar to those obtained in a single-stage reactor (Hudcova et al., 1989; You et al., 2014).
333 Lastly, the power consumption of the upper A310 impeller was independent of the bottom impeller
334 design (data not shown), which confirmed that both impellers were not interacting with each other.
335 The CFD simulations also showed that the power dissipation calculated by the turbulence model was,
336 on average over all configurations, equal to 58 % of the power consumption determined by the torque
337 of the impeller. This result is in accordance with most CFD simulations carried-out with the $k - \varepsilon$
338 turbulence model (Ochieng and Onyango, 2008).

339 As shown by Loubière et al. (2019) for various designs of impellers, the particle just-suspended state is
340 clearly related to the total power consumption per unit of volume P_{tot}/V , which considers the power
341 demand of both impellers. Thus, the values of this parameter were evaluated for the different impeller
342 configurations in order to determine the best configuration in term of particle suspension, at a given
343 agitation rate (Fig. 5). The results showed that, independently of the agitation rate, the configurations
344 with a bottom axial impeller (HTPGd and EEd) consumed less energy than the configurations with a
345 bottom radial impeller (RT4B, RT6B and R600). This agreed with the relative power numbers given in
346 Table 1 and with the experimental results reported by Bouaifi and Roustan (2001) and Wang et al.
347 (2010).

348



349

350 Fig. 5: Variation of the total power consumption per unit volume P_{tot}/V with the agitation rate, for
 351 each impeller configuration. Particle concentration was 10 % w/w.

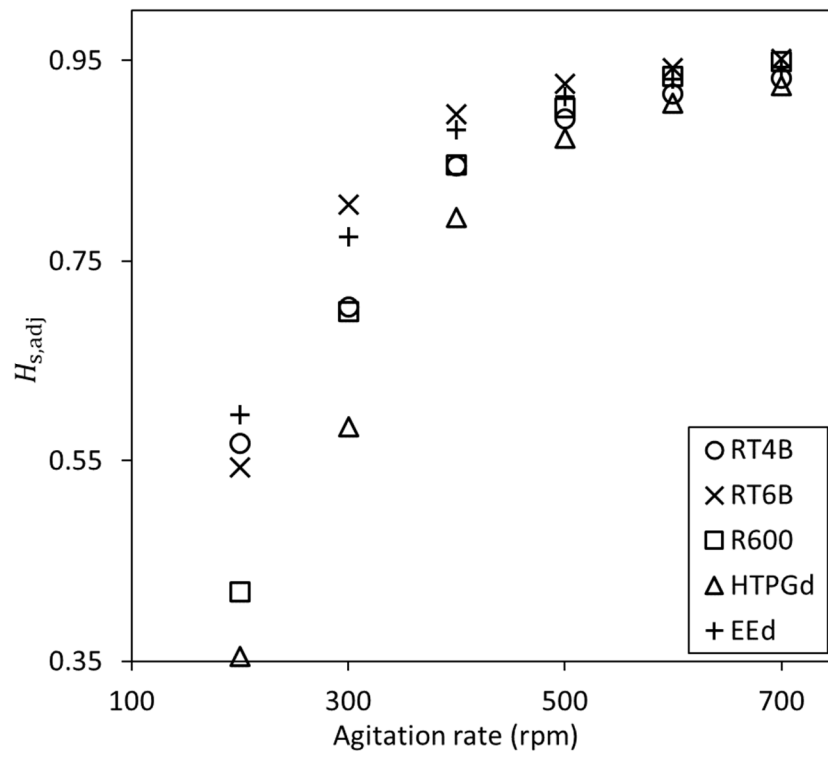
352

3.3. Particle mixing degree

353

To determine the particle mixing degree, the values of $H_{s,adj}$ were calculated for each configuration
 354 and operating condition of the bioreactor (Fig. 6). The values obtained showed a logarithmic increase
 355 with the agitation rate, with values ranging from 35 to 95 %. All configurations showed the same shape
 356 of particle mixing profile but with non-negligible relative differences, especially at low agitation rates.
 357 These differences were up to 40 % at 200 rpm between HTPGd and RT6B impellers but less than 10 %
 358 at 500 rpm and below. Independently of the agitation rate, both the RT6B and the EEd were the best
 359 to scatter particles throughout the tank at a given agitation rate. On the other hand, the HTPGd was
 360 the less efficient impeller in term of solid homogenization, with the lowest $H_{s,adj}$ for all the simulated
 361 agitation rates. This was emphasized by the discrepancies observed on the particle distribution, as
 362 shown by Fig. 7 (a-b) for 400 rpm. While for the RT6B impeller, the just-suspended state was clearly
 363 observed, the suspension of particles was still partial in the case of the HTPGd impeller, as indicated
 364 by the occurrence of settled particles ($\alpha_{s,max} = 0.82$ w/w) near the vessel bottom. Moreover, the
 365 radial impellers clearly showed a higher efficiency at bringing the particles upward (Fig. 7a), making
 366 the particle bed evolves to a cone shape at high agitation rate while the axial impellers promoted a
 367 pseudo-planar shape of particle bed.

368

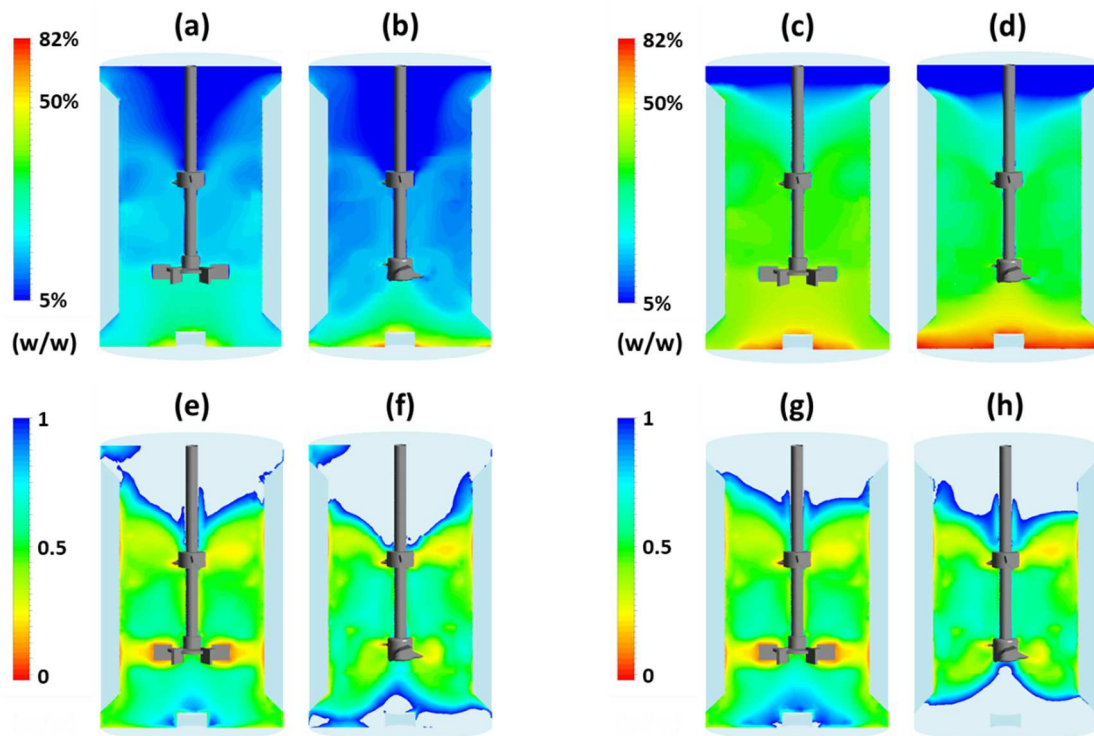


369

370 Fig. 6: Suspension quality $H_{s,adj}$ for each impeller configuration. Particle concentration was 10 % w/w.

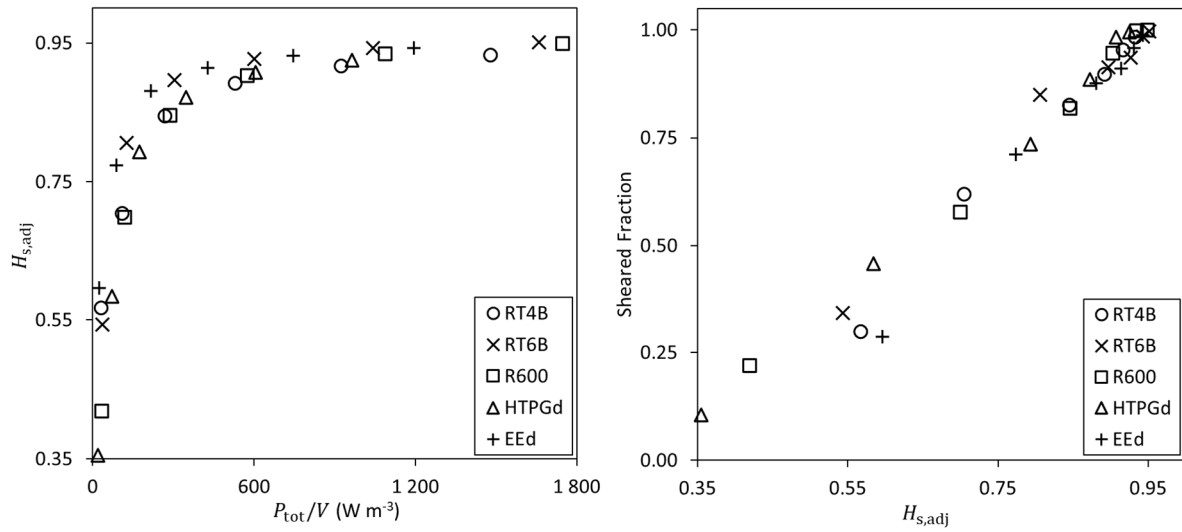
371

372



373 Fig. 7: Simulated particles distribution at $N = 400$ rpm for: (a) RT6B-A310 configuration with 10 % w/w
 374 solid; (b) HTPGd-A310 configuration with 10 % w/w solid; (c) RT6B-A310 configuration with 26 % w/w
 375 solid; (d) HTPGd-A310 configuration with 26 % w/w solid. Comparison of the particle size with the
 376 Kolmogorov length scale (l_K/d_p) for: (e) RT6B-A310 configuration with 10 % w/w solid; (f) HTPGd-A310
 377 configuration with 10 % w/w solid; (g) RT6B-A310 configuration with 26 % w/w solid; (h) HTPGd-A310
 378 configuration with 26 % w/w solid.

379 Aiming at determining a robust design criterion, the suspension quality $H_{s,adj}$ variation with the total
 380 power dissipation per unit volume was also determined (Fig. 8a). This variation could be divided into
 381 two zones. For power dissipation per unit of volume less than 600 W m^{-3} approximately, the parameter
 382 $H_{s,adj}$ rapidly increased till a value of $H_{s,adj} \approx 0.90$; regarding the particles distribution obtained for
 383 this range of power dissipation, only partial suspension was determined. For P_{tot}/V higher than 600
 384 W m^{-3} , the value of $H_{s,adj}$ slowly increased till 0.95 approximately, indicating a progressive particle
 385 homogenization beyond the just-suspended state. Thus, a substantial increase of mechanical energy
 386 consumption is required to achieve a minor enhancement of the particle homogenization. Moreover,
 387 it was also shown that total homogeneity ($H_{s,adj} = 1.0$) is not achievable as all the data tend to stagnate
 388 below $H_{s,adj} = 0.95$. This could be explained by the fact that, even for high power dissipations per unit
 389 of volume, a small region near the free surface remained free or poorly concentrated in particles, as
 390 demonstrated by Delafosse et al. (2018). Lastly, it is interesting to note that, for a given power
 391 dissipation per unit of volume, the variations of $H_{s,adj}$ were approximately independent of the
 392 bioreactor designs, meaning that power dissipation per unit of volume could be used not only as scaling
 393 parameter for particles just-suspended state determination but also to predict the quality of particles
 394 homogenization. Previous experiments by Magelli et al. (1991) have shown similar results in a single-
 395 stage vessel and pointed that it could be a basis for design optimization. Based on these results, it
 396 could be advised to promote the use an impeller which can achieve a high power dissipation per unit
 397 volume, even at the lowest agitation rate. This could indeed allow to get particle suspension at lower
 398 values of agitation rate and tip speed, which should limit the mechanical problems expected at high
 399 tip speeds.



401 Fig. 8: Solid distribution $H_{s,adj}$ as a function of power dissipation per unit volume P_{tot}/V (left) ;
 402 Suspension quality $H_{s,adj}$ as a function of the sheared fraction (right). Particle concentration was 10 %
 403 w/w.
 404

405 3.4. Particle stress

406 As discussed in the introductory part, it is generally assumed that only the turbulent eddies of the same
 407 order of length or lower than the particle size are potentially detrimental to the particles and thus **the**
 408 **microbial adhesion and** biofilm formation. Henzler (2000) stated that turbulent eddies of the same size
 409 of the particles are the most likely to damage the particles. In this case, namely some turbulent eddies
 410 are lower than the particle diameter, particles are transported in the inertial subrange of turbulence
 411 and are subjected to turbulent stresses. To quantify the relationships between particle stress and
 412 hydrodynamics, Thomas (1964) provided the expression of particle stress as related to the local mean
 413 square fluctuating liquid velocities $\overline{u_1'}$.

$$\sigma_p = \rho_1 \overline{u_1'^2} = 0.7 \rho_1 (\varepsilon d_p)^{2/3} \propto \varepsilon^{2/3} \quad (29)$$

414 In isotropic and homogeneous turbulence, the local mean square fluctuating liquid velocities depends
 415 on the local turbulent dissipation rate ε and on particle diameter d_p . If $d_p < l_K$, the particles are
 416 transported in the viscous subrange of the turbulence and are mainly subjected to viscous stresses
 417 given by:

$$\sigma_p = \mu G = \mu \sqrt{\frac{\varepsilon}{\nu_1}} \propto \varepsilon^{1/2} \quad (30)$$

418 with G (s⁻¹) the local velocity gradient.

419 From the preceding results, it appears clear that the determination of hydromechanical stresses acting
 420 on particles when suspended in the mixing tank should be determined locally and considering the
 421 relative ratio of the particle size on the Kolmogorov length scale. Thus, it was proposed here to assert
 422 the hydromechanical stress by calculating the sheared fraction SF (eq. 31), representing the
 423 percentage of particles volume under sheared conditions, namely in areas showing Kolmogorov scales
 424 lower than the particle diameter ($l_K < d_p$).

$$SF = \frac{1}{V_s} \cdot \iiint_{V_s(l_K < d_p)} dV_s = \frac{1}{V_s} \cdot \iiint_{V_s(l_K < d_p)} \alpha_s \cdot dV \quad (31)$$

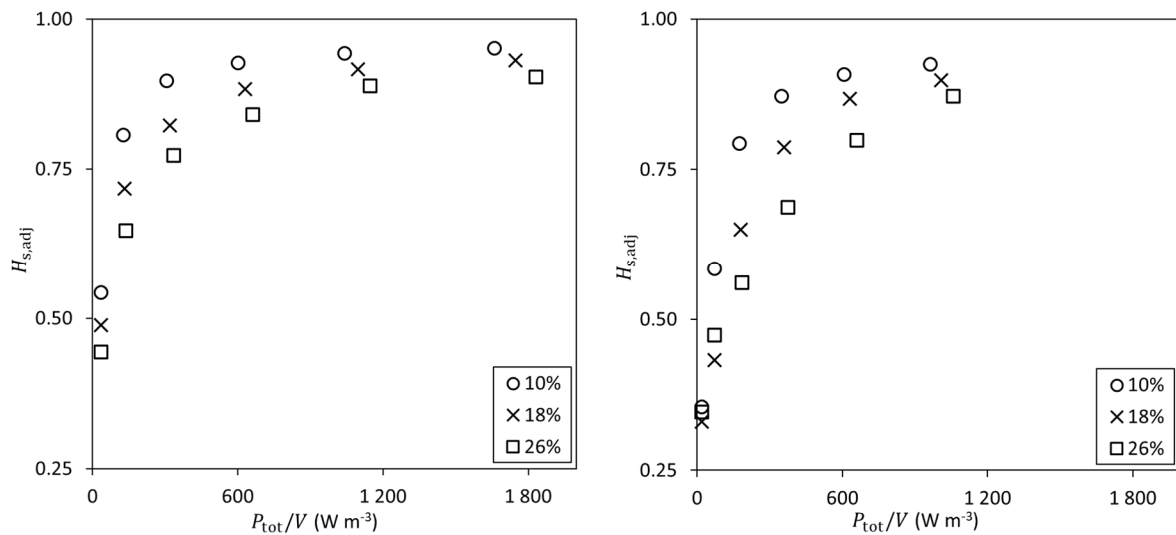
425 The variation of the sheared fraction SF with the suspension quality $H_{s,adj}$ was reported in Fig. 8. As
 426 one could expect, the stress on particles was growing higher as the suspension quality increased. You
 427 et al. (2020) obtained similar results using bioleaching continuous STR and reported that it was clearly
 428 linked to the mechanical forces acting on microbial productivity through the damaging mechanisms
 429 explained in this work. The variation of SF also showed that all the impeller designs presented the same
 430 linear evolution of SF, meaning that all the configurations would generate a similar particle stress for
 431 a given suspension quality. This could be partially explained by the previous results that put into
 432 evidence the relation between particle homogenization and total power demand. It is also interesting
 433 to note that, reaching a quasi-consistent homogenization of the particles implied that almost all the
 434 particles would encounter potentially damaging turbulent eddies that could promote biofilm
 435 detachment. When particles were not homogeneously distributed in the bioreactor, it is also important
 436 to consider the spatial distribution of the Kolmogorov length scales l_K , as it differed from one impeller
 437 to another, as shown in Fig. 7e and Fig. 7f. In conclusion, despite each bioreactor configuration
 438 generated different turbulent dissipation fields, the physical link between flow velocity, turbulent
 439 dissipation and particle concentrations led to unique relationships between sheared fraction of
 440 particles and suspension quality, whatever the impeller used. This also potentially questions the
 441 existence of ‘shearing’ or ‘non-shearing’ impellers when the degree of homogenization is considered
 442 as comparison parameter.

443 3.5. Impact of particle concentrations on bioreactor hydrodynamics

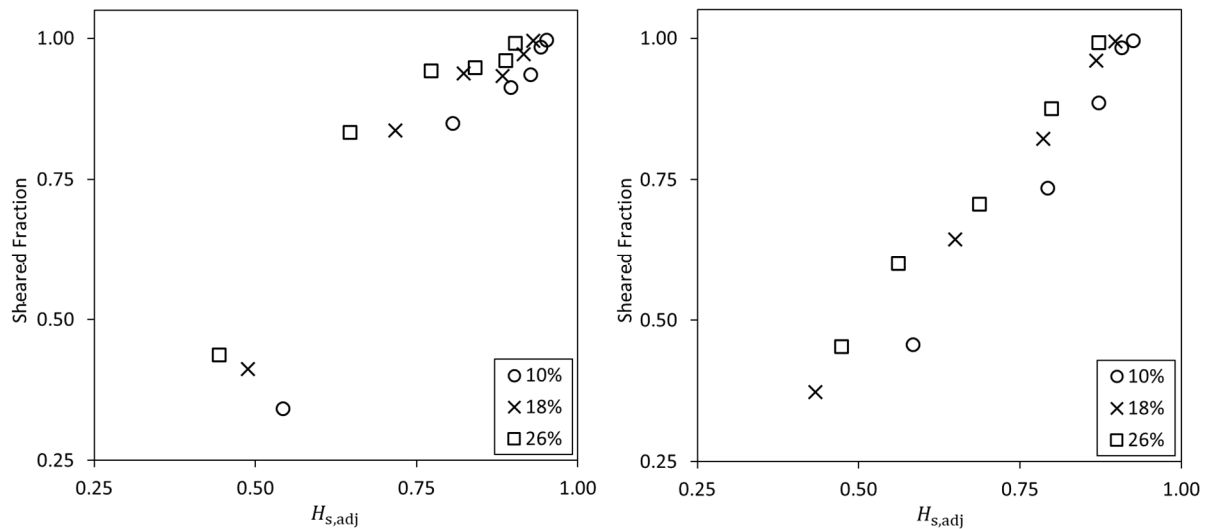
444 Considering that an increase of solid concentrations could potentially simultaneously promote an
 445 increase in bioprocess productivity and detrimental physical phenomena, the impact of solid
 446 concentration (from 10 to 18 and 26 % w/w) on bioreactor hydrodynamics was determined. For these
 447 simulations, only the designs RT6B-A310 and HTPGd-A310 were considered. First, regarding the just-
 448 suspended state of the particles, the basic Zwietering’s model predicts that the just-suspended
 449 agitation rate would be related to $N_{js} \propto X^{0.13}$. The influence of X on N_{js} was confirmed by the CFD
 450 simulations of the particles distributions generated by the RT6B and HTPGd configurations using solid
 451 concentrations of 10 and 26 % w/w as shown in Fig.7(a-d). Whereas no particle accumulation was
 452 observed for a particle loading of 10 % w/w at an agitation rate of 400 rpm for the RT6B impeller,
 453 settled particles were predicted by the simulations at the same agitation rate for a solid concentration
 454 of 26 % w/w, indicating that the agitation rate switched below N_{js} (Fig.7a and Fig 7c). For the HTPGd
 455 impeller, the small accumulation observed for a solid concentration of 10 % was clearly magnified for
 456 a solid concentration of 26 % (Fig. 7b and Fig. 7d). Considering the Zwietering’s model, for a constant
 457 power number expected in the turbulent regime, the total power demand at the just-suspended state
 458 would be $P_{js} \propto N_{js}^3 \propto X^{0.4}$. On the basis of this global scaling law, the power demand for a mean solid
 459 concentration of 26 % would be $P_{js}^{26\%} \simeq 1.55 \cdot P_{js}^{10\%}$.

460 The effect of the solid concentration on particle homogenization is shown in Fig. 9 for RT6B-A310 and
 461 HTPGd-A310 configurations. For both of them, the CFD simulation results confirmed that the increase
 462 in solid concentration led to a rise of power demand per unit volume to reach a given suspension
 463 quality. Moreover, it was also put into evidence that the asymptotic value of $H_{s,adj}$, obtained for the
 464 highest P_{tot}/V considered in this study, was progressively reduced as long as the solid concentration
 465 increased. For comparison, the power needed to achieve $H_{s,adj} = 0.90$ with the RT6B was
 466 $(P_{tot}/V)_{26\%} \simeq 2 \cdot (P_{tot}/V)_{18\%} \simeq 6 \cdot (P_{tot}/V)_{10\%}$. A similar trend was observed for the HTPGd with a
 467 smaller increase of power demand as the solid concentration rose, for $H_{s,adj} = 0.87$, $(P_{tot}/V)_{26\%} \simeq$

468 $1.7 \cdot (P_{\text{tot}}/V)_{18\%} \approx 3 \cdot (P_{\text{tot}}/V)_{10\%}$. Considering the sheared fraction SF , it was shown that, for a
 469 given $H_{s,\text{adj}}$, a higher fraction of particles was transported in the inertial subrange at higher solid
 470 concentrations. However, for both configurations and the three solid concentrations, the parameter
 471 SF reached a value close to 1 for the highest degrees of homogenization $H_{s,\text{adj}}$ (Fig. 10). This could
 472 explained by the fact that, for the particles that were suspended, the local variations in solid
 473 concentration in the areas where $d_p > l_K$ were similar between 10 and 26 % w/w (Fig. 7 (e-h)). This
 474 was not true near the reactor bottom where settling was predicted for particle concentration of 26 %
 475 w/w and which explained the less efficient particle homogenization.



476
 477 Fig. 9: Solid distribution $H_{s,\text{adj}}$ as a function of power consumption per unit volume P_{tot}/V at different
 478 solid concentration for: (left) the RT6B-A310 configuration; (right) the HTPGd-A310 configuration.



479
 480 Fig. 10: Suspension quality $H_{s,\text{adj}}$ as a function of the sheared fraction at different solid concentration
 481 for: (left) the RT6B-A310 configuration; (right) the HTPGd-A310 configuration.

482
 483 **4. Conclusion**

484 The effect of the impeller design on the solid suspension was determined using 5 dual-impeller
 485 configurations and 3 solid concentrations. For this, the power consumption per unit of volume, the

486 mixing efficiency and the particle stress were characterized by 50 CFD numerical simulations and
487 theoretical models of particle stress.

488 The results indicated that the power demand per unit volume could be used to predict the suspension
489 quality as the variations of $H_{s,adj}$ were independent of the bioreactor design for a given P_{tot}/V .
490 However, due to higher power numbers, the impellers RT6B and EEd could achieve particle suspension
491 at lower agitation rates. Furthermore, it was shown that increasing the solid loading led to a significant
492 rise of the power consumption per unit volume to attain a given suspension quality. Lastly, the impact
493 of each configuration on particle stress was assessed and the results showed that particle stress was
494 independent of the reactor design at a given suspension quality. **Consequently, it is difficult to advise
495 a specific configuration and experimental conditions regarding particle stress when using the
496 suspension quality as an optimisation criterion.**

497 The choice of impeller design in a bioleaching STR is critical to ensure the best solid dispersion within
498 the tank while maintaining a low power consumption and limiting the impact of shear stress on
499 particles. For higher scales (pilot and industrial scales), the energy cost due to mixing represents a large
500 part of OPEX expenses and impeller optimization should be closely considered. Nonetheless, further
501 studies are still necessary to take into account the biological aspect of bioleaching and the impact of
502 the design and the agitation on biomass.

503

504 **Acknowledgments**

505 The authors acknowledge the Institut Carnot ICEEL and the Institut Carnot BRGM for their financial
506 support.

507 **Nomenclature**

Variables

a	distance between particles, m
C	impeller off bottom clearance, m
C_D	drag coefficient
$C_{\varepsilon 1}, C_{\varepsilon 2}, C_{\mu}$	constants in turbulent equations
C_w	impeller torque, $N\ m^{-1}$
D	impeller diameter, m
d_p	particle diameter, m
D	impeller diameter, m
e_{ss}	particle collision restitution coefficient
F	force per unit volume, $N\ m^{-3}$
g	acceleration of gravity, $m\ s^{-2}$
G	local velocity gradient, $m\ s^{-1}$
G_k	turbulence production
H	liquid height, m
H_s	suspension quality
k	turbulent kinetic energy, $m^2\ s^{-2}$
K	interphase exchange coefficient
l_K	Kolmogorov length scale, m
N	impeller speed, rpm
p	pressure, Pa
P	impeller power consumption, W
r_0	radial distribution function
S	spacing between both impellers, m
SF	sheared fraction
T	tank diameter, m
u	velocity, $m\ s^{-1}$

V	working volume, m ³
X	particle concentration, w/w
Greek Letters	
α	volume fraction
γ	diffusion coefficient
γ_{θ_s}	collisional dissipation of energy, m ² s ⁻²
δ	turbulent Prandtl number
ε	turbulence eddy dissipation rate, m ² s ⁻³
θ_s	granular temperature, m ² s ⁻²
μ	viscosity, Pa s
ν	kinematic viscosity, m ² s ⁻¹
ρ	density, kg m ⁻³
σ_p	particle stress
$\bar{\tau}$	stress strain tensor, Pa
Φ	transfer of fluctuating energy, m ² s ⁻²

Dimensionless number

N_p	Power number
Re	Reynolds number

Subscripts

adj	adjusted
col	collisional
D	drag
diss	dissipated
js	just-suspended state
kin	kinetic
l	liquid phase
ls	action between liquid and solid
max	maximal
p	particle
s	solid phase
t	turbulence
tot	total
TD	turbulent dispersion
v	volume
w	weight

Abbreviations

A310	Lightnin A310 impeller
CFD	computational fluid dynamics
EEd	Elephant-Ear down impeller
HTPGd	HTPG down impeller
RT4B	4-bladed Rushton turbine
RT6B	6-bladed Rushton turbine
R600	R600 spiral backswept impeller
STR	stirred tank reactor

508

509

References

510 Bouaifi, M., Roustan, M., 2001. Power consumption, mixing time and homogenisation energy in dual-
511 impeller agitated gas–liquid reactors. *Chem. Eng. Process.: Process Intensif.* 40, 87–95.
512 [https://doi.org/10.1016/S0255-2701\(00\)00128-8](https://doi.org/10.1016/S0255-2701(00)00128-8)

513 Bouquet, F., Morin, D., 2006. BROGIM®: A new three-phase mixing system testwork and scale-up.
514 *Hydrometall., 16th International Biohydrometallurgy Symposium* 83, 97–105.
515 <https://doi.org/10.1016/j.hydromet.2006.03.040>

516 Brierley, C.L., Brierley, J.A., 2013. Progress in bioleaching: part B: applications of microbial processes
517 by the minerals industries. *Appl. Microbiol. Biotechnol.* 97, 7543–7552.
518 <https://doi.org/10.1007/s00253-013-5095-3>

519 Brucato, A., Cipollina, A., Micale, G., Scargiali, F., Tamburini, A., 2010. Particle suspension in top-
520 covered unbaffled tanks. *Chem. Eng. Sci.* 65, 3001–3008.
521 <https://doi.org/10.1016/j.ces.2010.01.026>

522 Buffo, M.M., Corrêa, L.J., Esperança, M.N., Cruz, A.J.G., Farinas, C.S., Badino, A.C., 2016. Influence of
523 dual-impeller type and configuration on oxygen transfer, power consumption, and shear rate
524 in a stirred tank bioreactor. *Biochemical Engineering Journal* 114, 130–139.
525 <https://doi.org/10.1016/j.bej.2016.07.003>

526 Bujalski, W., Takenaka, K., Paoleni, S., Jahoda, M., Paglianti, A., Takahashi, K., Nienow, A.W., Etchells,
527 A.W., 1999. Suspension and Liquid Homogenization in High Solids Concentration Stirred
528 Chemical Reactors. *Chemical Engineering Research and Design, Process and Product*
529 *Development* 77, 241–247. <https://doi.org/10.1205/026387699526151>

530 Chapple, D., Kresta, S.M., Wall, A., Afacan, A., 2002. The Effect of Impeller and Tank Geometry on
531 Power Number for a Pitched Blade Turbine. *Chem. Eng. Res. Des.* 80, 364–372.
532 <https://doi.org/10.1205/026387602317446407>

533 Clark, M.E., Batty, J.D., van Buuren, C.B., Dew, D.W., Eamon, M.A., 2006. Biotechnology in minerals
534 processing: Technological breakthroughs creating value. *Hydrometall., 16th International*
535 *Biohydrometallurgy Symposium* 83, 3–9. <https://doi.org/10.1016/j.hydromet.2006.03.046>

536 d’Hugues, P., Foucher, S., Gallé-Cavalloni, P., Morin, D., 2002. Continuous bioleaching of chalcopyrite
537 using a novel extremely thermophilic mixed culture. *International Journal of Mineral*
538 *Processing* 66, 107–119. [https://doi.org/10.1016/S0301-7516\(02\)00004-2](https://doi.org/10.1016/S0301-7516(02)00004-2)

539 d’Hugues, P., Jouliau, C., Spolaore, P., Michel, C., Garrido, F., Morin, D., 2008. Continuous bioleaching
540 of a pyrite concentrate in stirred reactors: Population dynamics and exopolysaccharide
541 production vs. bioleaching performance. *Hydrometallurgy, 17th International*
542 *Biohydrometallurgy Symposium, IBS 2007, Frankfurt a.M., Germany, 2-5 September 2007* 94,
543 34–41. <https://doi.org/10.1016/j.hydromet.2008.05.045>

544 Delafosse, A., Loubière, C., Calvo, S., Toye, D., Olmos, E., 2018. Solid-liquid suspension of
545 microcarriers in stirred tank bioreactor – Experimental and numerical analysis. *Chem. Eng.*
546 *Sci.* 180, 52–63. <https://doi.org/10.1016/j.ces.2018.01.001>

547 Ding, J., Gidaspow, D., 1990. A bubbling fluidization model using kinetic theory of granular flow.
548 *AIChE J.* 36, 523–538. <https://doi.org/10.1002/aic.690360404>

549 Frenzel, M., Kullik, J., Reuter, M.A., Gutzmer, J., 2017. Raw material ‘criticality’—sense or nonsense?
550 *J. Phys. D: Appl. Phys.* 50, 123002. <https://doi.org/10.1088/1361-6463/aa5b64>

551 Furukawa, H., Kato, Y., Inoue, Y., Kato, T., Tada, Y., Hashimoto, S., 2012. Correlation of Power
552 Consumption for Several Kinds of Mixing Impellers. *Int. J. Chem. Eng.* 2012, 1–6.
553 <https://doi.org/10.1155/2012/106496>

554 Gradov, D.V., González, G., Vauhkonen, M., Laari, A., Koironen, T., 2017. Experimental and Numerical
555 Study of Multiphase Mixing Hydrodynamics in Batch Stirred Tank Applied to Ammoniacal
556 Thiosulphate Leaching of Gold. *J. Chem. Eng. Process Technol.* 08.
557 <https://doi.org/10.4172/2157-7048.1000348>

558 Guezennec, A.-G., Jouliau, C., Jacob, J., Archane, A., Ibarra, D., de Buyer, R., Bodéan, F., d’Hugues, P.,
559 2017. Influence of dissolved oxygen on the bioleaching efficiency under oxygen enriched
560 atmosphere. *Miner. Eng., Biohydrometallurgy* 106, 64–70.
561 <https://doi.org/10.1016/j.mineng.2016.10.016>

562 Harrison, S.T.L., Stevenson, R., Cilliers, J.J., 2012. Assessing solids concentration homogeneity in
563 Rushton-agitated slurry reactors using electrical resistance tomography (ERT). *Chem. Eng.*
564 *Sci.* 71, 392–399. <https://doi.org/10.1016/j.ces.2011.10.053>
565 Henzler, H.-J., 2000. Particle Stress in Bioreactors, in: Schügerl, K., Kretzmer, G., Henzler, H.J., Kieran,
566 P.M., Kretzmer, G., MacLoughlin, P.E., Malone, D.M., Schumann, W., Shamlou, P.A., Yim, S.S.
567 (Eds.), *Influence of Stress on Cell Growth and Product Formation, Advances in Biochemical*
568 *Engineering/Biotechnology*. Springer, Berlin, Heidelberg, pp. 35–82.
569 https://doi.org/10.1007/3-540-47865-5_2
570 Hosseini, S., Patel, D., Ein-Mozaffari, F., Mehrvar, M., 2010. Study of Solid–Liquid Mixing in Agitated
571 Tanks through Computational Fluid Dynamics Modeling. *Ind. Eng. Chem. Res.* 49, 4426–4435.
572 <https://doi.org/10.1021/ie901130z>
573 Houcine, I., Plasari, E., David, R., 2000. Effects of the Stirred Tank’s Design on Power Consumption
574 and Mixing Time in Liquid Phase. *Chem. Eng. Technol.* 23, 605–613.
575 [https://doi.org/10.1002/1521-4125\(200007\)23:7<605::AID-CEAT605>3.0.CO;2-0](https://doi.org/10.1002/1521-4125(200007)23:7<605::AID-CEAT605>3.0.CO;2-0)
576 Hudcova, V., Machon, V., Nienow, A.W., 1989. Gas–liquid dispersion with dual Rushton impellers.
577 *Biotechnol. Bioeng.* 34, 617–628. <https://doi.org/10.1002/bit.260340506>
578 Jafari, R., Tanguy, P.A., Chaouki, J., 2012. Experimental investigation on solid dispersion, power
579 consumption and scale-up in moderate to dense solid–liquid suspensions. *Chemical*
580 *Engineering Research and Design* 90, 201–212. <https://doi.org/10.1016/j.cherd.2011.07.009>
581 Jenkins, J.T., Savage, S.B., 1983. A theory for the rapid flow of identical, smooth, nearly elastic,
582 spherical particles. *J. Fluid. Mech.* 130, 187–202.
583 <https://doi.org/10.1017/S0022112083001044>
584 Kasat, G.R., Pandit, A.B., Ranade, V.V., 2008. CFD Simulation of Gas-Liquid Flows in a Reactor Stirred
585 by Dual Rushton Turbines. *Int. J. Chem. React. Eng.* 6. [https://doi.org/10.2202/1542-](https://doi.org/10.2202/1542-6580.1628)
586 [6580.1628](https://doi.org/10.2202/1542-6580.1628)
587 Khopkar, A.R., Kasat, G.R., Pandit, A.B., Ranade, V.V., 2006. Computational Fluid Dynamics Simulation
588 of the Solid Suspension in a Stirred Slurry Reactor. *Ind. Eng. Chem. Res.* 45, 4416–4428.
589 <https://doi.org/10.1021/ie050941q>
590 Kumaresan, T., Joshi, J.B., 2006. Effect of impeller design on the flow pattern and mixing in stirred
591 tanks. *Chem. Eng. J.* 115, 173–193. <https://doi.org/10.1016/j.ces.2005.10.002>
592 Ljungqvist, M., Rasmuson, A., 2001. Numerical Simulation of the Two-Phase Flow in an Axially Stirred
593 Vessel. *Chem. Eng. Res. Des., Fluid Flow* 79, 533–546.
594 <https://doi.org/10.1205/02638760152424307>
595 Loubière, C., Delafosse, A., Guedon, E., Toye, D., Chevalot, I., Olmos, E., 2019. Optimization of the
596 Impeller Design for Mesenchymal Stem Cell Culture on Microcarriers in Bioreactors. *Chem.*
597 *Eng. Technol.* 42, 1702–1708. <https://doi.org/10.1002/ceat.201900105>
598 Magelli, F., Fajner, D., Nocentini, M., Pasquali, G., Marisko, V., Dittl, P., 1991. Solids concentration
599 distribution in slurry reactors stirred with multiple axial impellers. *Chem. Eng. Process.:*
600 *Process Intensif.* 29, 27–32. [https://doi.org/10.1016/0255-2701\(91\)87003-L](https://doi.org/10.1016/0255-2701(91)87003-L)
601 Mak, A.T.-C., 1992. Solid-liquid mixing in mechanically agitated vessels (Doctoral). Doctoral thesis,
602 University of London. University of London.
603 Montante, G., Paglianti, A., Magelli, F., 2012. Analysis of dilute solid–liquid suspensions in turbulent
604 stirred tanks. *Chem. Eng. Res. Des.* 90, 1448–1456.
605 <https://doi.org/10.1016/j.cherd.2012.01.009>
606 Morin, D.H.R., d’Hugues, P., 2007. Bioleaching of a Cobalt-Containing Pyrite in Stirred Reactors: a
607 Case Study from Laboratory Scale to Industrial Application, in: Rawlings, D.E., Johnson, D.B.
608 (Eds.), *Biomining*. Springer, Berlin, Heidelberg, pp. 35–55. [https://doi.org/10.1007/978-3-](https://doi.org/10.1007/978-3-540-34911-2_2)
609 [540-34911-2_2](https://doi.org/10.1007/978-3-540-34911-2_2)
610 Mudd, G.M., Weng, Z., Jowitt, S.M., 2013. A Detailed Assessment of Global Cu Resource Trends and
611 Endowments. *Econ. Geol.* 108, 1163–1183. <https://doi.org/10.2113/econgeo.108.5.1163>
612 Murthy, B.N., Ghadge, R.S., Joshi, J.B., 2007. CFD simulations of gas–liquid–solid stirred reactor:
613 Prediction of critical impeller speed for solid suspension. *Chemical Engineering Science*, 8th

614 International Conference on Gas-Liquid and Gas-Liquid-Solid Reactor Engineering 62, 7184–
615 7195. <https://doi.org/10.1016/j.ces.2007.07.005>

616 Neale, J., Seppälä, J., Laukka, A., Aswegen, P., Barnett, S., Gericke, M., 2017. The MONDO Minerals
617 Nickel Sulfide Bioleach Project: From Test Work to Early Plant Operation. *Solid State Phenom.*
618 262, 28–32. <https://doi.org/10.4028/www.scientific.net/SSP.262.28>

619 Nemati, M., Harrison, S.T.L., 2000. Effect of solid loading on thermophilic bioleaching of sulfide
620 minerals. *Journal of Chemical Technology & Biotechnology* 75, 526–532.
621 [https://doi.org/10.1002/1097-4660\(200007\)75:7<526::AID-JCTB249>3.0.CO;2-4](https://doi.org/10.1002/1097-4660(200007)75:7<526::AID-JCTB249>3.0.CO;2-4)

622 Nienow, A.W., 2006. Reactor Engineering in Large Scale Animal Cell Culture. *Cytotechnol.* 50, 9.
623 <https://doi.org/10.1007/s10616-006-9005-8>

624 Ochieng, A., Onyango, M.S., 2008. Homogenization energy in a stirred tank. *Chem. Eng. Process.:
625 Process Intensif.* 47, 1853–1860. <https://doi.org/10.1016/j.cep.2007.10.014>

626 Petersen, J., 2010. Modelling of bioleach processes: Connection between science and engineering.
627 *Hydrometall.*, 18th International Biohydrometallurgy Symposium, IBS2009, Bariloche-
628 Argentina, 13-17 September 2009 104, 404–409.
629 <https://doi.org/10.1016/j.hydromet.2010.02.023>

630 Qi, N., Zhang, H., Zhang, K., Xu, G., Yang, Y., 2013. CFD simulation of particle suspension in a stirred
631 tank. *Particuology* 11, 317–326. <https://doi.org/10.1016/j.partic.2012.03.003>

632 Raja Ehsan Shah, R.S.S., Sajjadi, B., Abdul Raman, A.A., Ibrahim, S., 2015. Solid-liquid mixing analysis
633 in stirred vessels. *Rev. Chem. Eng.* 31. <https://doi.org/10.1515/revce-2014-0028>

634 Raja, S., 2005. The effect of particulate-induced hydrodynamic stress on the bioleaching of
635 chalcopyrite by a *Sulfolobus* sp.

636 Rawlings, D.E., Johnson, D.B., 2007. The microbiology of biomining: development and optimization of
637 mineral-oxidizing microbial consortia. *Microbiol.* 153, 315–324.
638 <https://doi.org/10.1099/mic.0.2006/001206-0>

639 Rodríguez, Y., Ballester, A., Blázquez, M.L., González, F., Muñoz, J.A., 2003. Study of Bacterial
640 Attachment During the Bioleaching of Pyrite, Chalcopyrite, and Sphalerite. *Geomicrobiology
641 Journal* 20, 131–141. <https://doi.org/10.1080/01490450303880>

642 Roustan, M., 2005. Agitation. *Mélange - Caractéristiques des mobiles d'agitation.* *Tech. Ing.*

643 Rushton, J.H., 1950. Power Characteristics of Mixing Impellers Part 1. *Chem. Eng. Prog.* 46, 395–404.

644 Schiller, L., 1933. A Drag Coefficient Correlation. *Zeit. Ver. Deutsch. Ing.* 77, 318–320.

645 Sissing, A., Harrison, S.T.L., 2003. Thermophilic mineral bioleaching performance: A compromise
646 between maximizing mineral loading and maximizing microbial growth and activity. *J. South.
647 Afr. Inst. Min. Metall.* 4.

648 s.n. Ansys, 2019. *Fluent Theory Guide* 962.

649 Song, T., Jiang, K., Zhou, J., Wang, D., Xu, N., Feng, Y., 2015. CFD modelling of gas–liquid flow in an
650 industrial scale gas-stirred leaching tank. *Int. J. Miner. Process., Mineral processing in
651 Australia and China* 142, 63–72. <https://doi.org/10.1016/j.minpro.2015.01.005>

652 Tamburini, A., Brucato, A., Cipollina, A., Micale, G., Ciofalo, M., 2012. CFD Predictions of Sufficient
653 Suspension Conditions in Solid-Liquid Agitated Tanks. *Int. J. Nonlinear Sci. Numer. Simul.* 13.
654 <https://doi.org/10.1515/ijnsns-2012-0027>

655 Tamburini, A., Cipollina, A., Micale, G., Brucato, A., Ciofalo, M., 2014. Influence of drag and
656 turbulence modelling on CFD predictions of solid liquid suspensions in stirred vessels. *Chem.
657 Eng. Res. Des.* 92, 1045–1063. <https://doi.org/10.1016/j.cherd.2013.10.020>

658 Tamburini, A., Cipollina, A., Micale, G., Brucato, A., Ciofalo, M., 2011. CFD simulations of dense solid–
659 liquid suspensions in baffled stirred tanks: Prediction of suspension curves. *Chem. Eng. J.*
660 178, 324–341. <https://doi.org/10.1016/j.cej.2011.10.016>

661 Tatterson, G.B., 1991. *Fluid Mixing and Gas Dispersion in Agitated Tanks.* McGraw-Hill.

662 Thomas, D.G., 1964. Turbulent disruption of flocs in small particle size suspensions. *AIChE J.* 10, 517–
663 523. <https://doi.org/10.1002/aic.690100420>

664 Vrabel, P., van der Lans, R.G.J.M., Luyben, K.Ch.A.M., Boon, L., Nienow, A.W., 2000. Mixing in large-
665 scale vessels stirred with multiple radial or radial and axial up-pumping impellers: modelling

666 and measurements. *Chem. Eng. Sci.* 55, 5881–5896. <https://doi.org/10.1016/S0009->
667 2509(00)00175-5

668 Wadnerkar, D., Utikar, R.P., Tade, M.O., Pareek, V.K., 2012. CFD simulation of solid–liquid stirred
669 tanks. *Adv. Powder Technol.* 23, 445–453. <https://doi.org/10.1016/j.appt.2012.03.007>

670 Wakeman, K.D., Honkavirta, P., Puhakka, J.A., 2011. Bioleaching of flotation by-products of talc
671 production permits the separation of nickel and cobalt from iron and arsenic. *Process*
672 *Biochem.* 46, 1589–1598. <https://doi.org/10.1016/j.procbio.2011.04.016>

673 Wang, T., Yu, G., Yong, Y., Yang, C., Mao, Z.-S., 2010. Hydrodynamic Characteristics of Dual-Impeller
674 Configurations in a Multiple-Phase Stirred Tank. *Ind. Eng. Chem. Res.* 49, 1001–1009.
675 <https://doi.org/10.1021/ie9006886>

676 Wang, Y., Su, L., Zeng, W., Wan, L., Chen, Z., Zhang, L., Qiu, G., Chen, X., Zhou, H., 2014. Effect of pulp
677 density on planktonic and attached community dynamics during bioleaching of chalcopyrite
678 by a moderately thermophilic microbial culture under uncontrolled conditions. *Miner. Eng.*
679 61, 66–72. <https://doi.org/10.1016/j.mineng.2014.03.012>

680 Witne, J.Y., Phillips, C.V., 2001. Bioleaching of Ok Tedi copper concentrate in oxygen- and carbon
681 dioxide-enriched air. *Miner. Eng.* 14, 25–48. [https://doi.org/10.1016/S0892-6875\(00\)00158-8](https://doi.org/10.1016/S0892-6875(00)00158-8)

682 Xia, L., Liu, X., Zeng, J., Yin, C., Gao, J., Liu, J., Qiu, G., 2008. Mechanism of enhanced bioleaching
683 efficiency of *Acidithiobacillus ferrooxidans* after adaptation with chalcopyrite. *Hydrometall.*
684 92, 95–101. <https://doi.org/10.1016/j.hydromet.2008.01.002>

685 You, J., Solongo, S.K., Gomez-Flores, A., Choi, S., Zhao, H., Urík, M., Ilyas, S., Kim, H., 2020. Intensified
686 bioleaching of chalcopyrite concentrate using adapted mesophilic culture in continuous
687 stirred tank reactors. *Bioresource Technology* 307, 123181.
688 <https://doi.org/10.1016/j.biortech.2020.123181>

689 You, S.T., Raman, A.A.A., Shah, R.S.S.R.E., Mohamad Nor, M.I., 2014. Multiple-impeller stirred vessel
690 studies. *Rev. Chem. Eng.* 30. <https://doi.org/10.1515/revce-2013-0028>

691 Zhang, J., Gao, Z., Cai, Y., Cao, H., Cai, Z., Bao, Y., 2017. Power consumption and mass transfer in a
692 gas-liquid-solid stirred tank reactor with various triple-impeller combinations. *Chem. Eng.*
693 *Sci.*, 13th International Conference on Gas-Liquid and Gas-Liquid-Solid Reactor Engineering
694 170, 464–475. <https://doi.org/10.1016/j.ces.2017.02.002>

695 Zheng, C., Guo, J., Wang, C., Chen, Y., Zheng, H., Yan, Z., Chen, Q., 2018a. Experimental study and
696 simulation of a three-phase flow stirred bioreactor. *Chin. J. Chem. Eng.*
697 <https://doi.org/10.1016/j.cjche.2018.06.010>

698 Zheng, C., Huang, Y., Guo, J., Cai, R., Zheng, H., Lin, C., Chen, Q., 2018b. Investigation of cleaner
699 sulfide mineral oxidation technology: Simulation and evaluation of stirred bioreactors for
700 gold-bioleaching process. *J. Clean. Prod.* 192, 364–375.
701 <https://doi.org/10.1016/j.jclepro.2018.04.172>

702 Zhu, H., Nienow, A.W., Bujalski, W., Simmons, M.J.H., 2009. Mixing studies in a model aerated
703 bioreactor equipped with an up- or a down-pumping ‘Elephant Ear’ agitator: Power, hold-up
704 and aerated flow field measurements. *Chem. Eng. Res. Des.* 87, 307–317.
705 <https://doi.org/10.1016/j.cherd.2008.08.013>

706 Zwietering, Th.N., 1958. Suspending of solid particles in liquid by agitators. *Chem. Eng. Sci.* 8, 244–
707 253. [https://doi.org/10.1016/0009-2509\(58\)85031-9](https://doi.org/10.1016/0009-2509(58)85031-9)

708